# Confining the sampling volume for Fluorescence Correlation Spectroscopy using a sub-wavelength sized aperture

**Marcel Leutenegger[1], Michael Gösch[1], Alexandre Perentes[2], Patrik Hoffmann[2], Olivier J.F. Martin[3], Theo Lasser[1]**

[1] *Laboratoire d'Optique Biomédicale, École Polytechnique Fédérale de Lausanne, 1015 Lausanne, Switzerland*

*http://lob.epfl.ch/*

[2] *Laboratoire d'Optique Appliquée, École Polytechnique Fédérale de Lausanne, 1015 Lausanne, Switzerland*

*http://apl.epfl.ch/*

[3] *Laboratoire de nanophotonique et métrologie, École Polytechnique Fédérale de Lausanne, 1015 Lausanne, Switzerland*

*http://www.nanophotonics.ch/*

**Abstract:** For the observation of single molecule dynamics with fluorescence fluctuation spectroscopy (FFS) very low fluorophore concentrations are necessary. For in vitro measurements, this requirement is easy to fulfill. In biology however, micromolar concentrations are often encountered and may pose a real challenge to conventional FFS methods based on confocal instrumentation. We show a higher confinement of the sampling volume in the near-field of sub-wavelength sized apertures in a thin gold film. The gold apertures have been measured and characterized with fluorescence correlation spectroscopy (FCS), indicating light confinement beyond the far-field diffraction limit. We measured a reduction of the effective sampling volume by an order of magnitude compared to confocal instrumentation.

## References and links

1. R. Rigler et al., "Fluorescence Correlation Spectroscopy with high Count Rate and low Background - Analysis of Translational Diffusion," Eur. Biophys. J. Biophys. Lett. **22,** 169–175 (1993).
2. S. Weiss, "Fluorescence Spectroscopy of Single Biomolecules," Science **283,** 1676–1683 (1999).
3. P. Kask, K. Palo, D. Ullmann, K. Gall, "Fluorescence-intensity distribution analysis and its application in biomolecular detection technology," PNAS **96,** 13756–13761 (1999).
4. Y. Chen, J.D. Müller, P.T.C. So, E. Gratton, "The Photon Counting Histogram in Fluorescence Fluctuation Spectroscopy," Biophys. J. **77,** 553–567 (1999).
5. L.N. Hillesheim, J.D. Müller, "The Photon Counting Histogram in Fluorescence Fluctuation Spectroscopy with Non-Ideal Photodetectors," Biophys. J. **85,** 1948–1958 (2003).
6. T.A. Laurence, A.N. Kapanidis, X. Kong, D.S. Chemla, S. Weiss, "Photon Arrival-Time Interval Distribution (PAID): A Novel Tool for Analyzing Molecular Interactions," J. Phys. Chem. B **108,** 3051–3067 (2004).

7.  K. Starchev, J. Ricka, J. Buffle, "Noise on Fluorescence Correlation Spectroscopy," J. Coll. Interf. Science **233,** 50–55 (2001).
8.  D.E. Koppel, "Statistical accuracy in fluorescence correlation spectroscopy," Phys. Rev. A **10,** 1938–1945 (1974).
9.  M.J. Levene, J. Korlach, S.W. Turner, M. Foquet, H.G. Craighead, W.W. Webb, "Zero-Mode Waveguides for Single-Molecule Analysis at High Concentrations," Science **299,** 682–686 (2003).
10. M. Foquet, J. Korlach, W.R. Zipfel, W.W. Webb, H.G. Craighead, "Focal Volume Confinement by Submicrometer-Sized Fluidic Channels," Anal. Chem. **76,** 1618–1626 (2004).
11. T. Ruckstuhl, S. Seeger, "Attoliter detection volumes by confocal total-internal-reflection fluorescence microscopy," Opt. Lett. **29,** 569–571 (2004).
12. K. Hassler, T. Anhut, R. Rigler, M. Gösch, T. Lasser, "High Count Rates with Total Internal Reflection Fluorescence Correlation Spectroscopy," Biophys. J. **88,** L1–L3 (2005).
13. K. Hassler, M. Leutenegger, P. Rigler, R. Rao, R. Rigler, M. Gösch, T. Lasser, "Total internal reflection fluorescence correlation spectroscopy (TIR-FCS) with low background and high count-rate per molecule," Opt. Express **13,** 7415–7423 (2005).
14. M. Paulus, O.J.F. Martin, "Light propagation and scattering in stratified media: a Green's tensor approach," J. Opt. Soc. Am. A **18,** 854–861 (2001).
15. H. Rigneault, J. Capoulade, J. Dintinger, J. Wenger, N. Bonod, E. Popov, T.W. Ebbesen, P.-F. Lenne, "Enhancement of Single-Molecule Fluorescence Detection in Subwavelength Apertures," Phys. Rev. Lett. **95,** 117401 (2005).
16. J. Wenger, P.-F. Lenne, E. Popov, H. Rigneault, J. Dintinger, T.W. Ebbesen, "Single molecule fluorescence in rectangular nano-apertures," Opt. Express **13,** 7035–7044 (2005).
17. D. Amarie, N.D. Rawlinson, W.L. Schaich, B. Dragnea, S.C. Jacobson, "Three-Dimensional Mapping of the Light Intensity Transmitted through Nanoapertures," Nanolett. **5,** 1227–1230 (2005).
18. A. Perentes, I. Utke, B. Dwir, M. Leutenegger, T. Lasser, P. Hoffmann, F. Baida, M.P. Bernal, M. Russey, J. Salvi, D. Van Labeke, "Fabrication of arrays of sub-wavelength nano-apertures in an optically thick gold layer on glass slides for optical studies," Nanotech. **16,** S273–S277 (2005).
19. O. Krichevsky, G. Bonnet, "Fluorescence correlation spectroscopy: the technique and its applications," Rep. Prog. Phys. **65,** 251–297 (2002).
20. K. Bacia, I.V. Majoul, P. Schwille, "Probing the endocytic pathway in live cells using dual-color fluorescence cross-correlation analysis," Biophys. J. **83,** 1184–1193 (2002).
21. J. Widgengren, Ü. Mets, R. Rigler, "Fluorescence correlation spectroscopy of triplet states in solution: A theoretical and experimental study," J. Phys. Chem. **99,** 13368–13379 (1995).
22. T. Wohland, R. Rigler, H. Vogel, "The Standard Deviation in Fluorescence Correlation Spectroscopy," Biophys. J. **80,** 2987–2999 (2001).
23. E. Bismuto, E. Gratton, D.C. Lamb, "Dynamics of ANS Binding to Tuna Apomyoglobin Measured with Fluorescence Correlation Spectroscopy," Biophys. J. **81,** 3510–3521 (2001).
24. J. Enderlein, I. Gregor, D. Patra, J. Fitter, "Art and artefacts of fluorescence correlation spectroscopy," Curr. Pharmaceut. Biotech. **5,** 155–161 (2004).
25. G.T. Boyd, Z.H. Yu, Y.R. Shen, "Photoinduced luminescence from the noble metals and its enhancement on roughned surfaces," Phys. Rev. B **33,** 7923–7936 (1986).
26. K. Kneipp, H. Kneipp, I. Itzkan, R.R. Dasari, M.S. Feld, "Surface-enhanced Raman scattering and biophysics," J. Phys. Condens. Matter **14,** R597–R624 (2002).

## 1. Introduction

In the last decade, fluorescence fluctuation spectroscopy (FFS) emerged as a powerful screening tool in pharmaceutical industry and in biomedical research. For FFS, a high numerical aperture objective focuses a laser beam into a sample containing labeled molecules at low concentration. The fluorescence is collected by the same objective and filtered by a dielectric band-pass filter to suppress reflected excitation and Raman scattered light. The fluorescence is focused onto a pinhole rejecting stray and out of focus light and keeping the Raman scattered light to a minimum. A single photon detector is used to count the photons, and the recorded photon trace is then evaluated according to the chosen FFS method [1–6].

The confocal setup provides a small sampling volume, an excellent signal to noise ratio (SNR), and good statistical accuracy. In vitro, the sample concentration is chosen to maximize the SNR [7, 8]. For instance, typical sampling volumes of 250 al and nanomolar concentrations of the analyte are mostly used. However, many reactions in biology or biochemistry demand measurements at micromolar concentrations. This results in a high number of labeled molecules

in the confocal volume, with in consequence a small fluctuation amplitude or a high photon number beyond the linear range of single photon detectors.

In order to perform these experiments, the size of the sampling volume needs a further reduction. Webb et al. addressed the problem by limiting the sampling volume in their setup to far less than 1 al by using nano-wells in an aluminium mask [9]. A potential drawback is the background from direct-reflected excitation light. Micro-channels in fused silica have been used as well and sampling volumes of less than 2 al were achieved [10]. Another approach took advantage of a parabolic mirror in a total internal reflection fluorescence correlation spectroscopy (TIR-FCS) setup, which resulted in a sampling volume of about 5 al [11]. Hassler et al. reported small sampling volumes of 60 al by taking advantage of a high numerical aperture objective (NA = 1.45) and an evanescent field excitation [12]. They showed a high SNR as well as high count rates per molecule (CPM) and used their setup for binding-unbinding studies as well as for investigations of enzyme reactions [13].

In this project, we fabricated sub-wavelength sized circular apertures in a thin gold film in order to reduce the sampling volume. Back-illumination of such an aperture results in a highly confined excitation field. With the Green's tensor technique [14], we calculated an excitation volume of about 7 al for an aperture with 150 nm diameter in a 150 nm thick gold film on top of a glass cover slip. This results in a reduction of the excitation volume by more than an order of magnitude. The detection volume is as for a conventional approach given by the confocal setup. The fluorescence is recorded from the volume in and just above the aperture while the metal mask shields most of the excitation light. Finally, the evaluation of the fluorescence signal provides information about the size of the excitation volume.

Fluorescence in the presence of a structured metal film is very dependent on the local excitation field, the local emission pattern, and the local fluorescence lifetime. Recently, Rigneault et al. reported an increased excitation intensity and a decreased fluorescence lifetime enhancing the CPM in circular aluminium nano-holes [15]. Using rectangular aluminium nano-apertures, Wenger et al. demonstrated that the enhancement is mainly due to a strong evanescent excitation field [16]. Here, we report on trans-illumination measurements collecting fluorescence within but mainly behind a circular nano-aperture. The local fluorescence emission would deserve further investigation but is out of the scope of this paper. Instead, we concentrate on the three-dimensional excitation field, which can also be mapped in detail with the help of a photoresist [17].

## 2. Experiment

### 2.1. Aperture masks

The circular apertures were fabricated with a focused electron beam lithography process [18]. A 170 $\mu$m glass cover slide was plasma cleaned and covered with 10 nm antimony doped tin oxide. The aperture structures were written into a spin coated high contrast negative tone resist. The resist was developed resulting in freestanding resist structures. These structures were coated with a titanium layer (5 nm) and with a 150 nm thick gold film. A final lift-off process resulted in the apertures shown in Fig. 1. Figure 2 outlines the layout of the entire gold mask. Within six fields, we fabricated a total of 144 arrays of 6×6 apertures. Each field was located and oriented with the help of triangular marks. We verified the dimensions of selected apertures by scanning electron microscopy (SEM). In addition, we checked all aperture arrays with an optical trans-illumination microscope (Carl Zeiss AxioVert 200m with Carl Zeiss AxioCam HRm). The inset in Fig. 2 shows the image of a homogeneous array used for measurements.
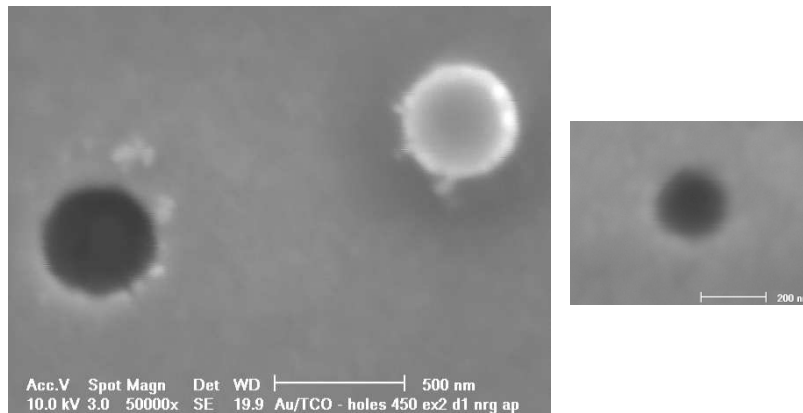
Fig. 1. Left: SEM image of a 420 nm aperture after evaporation of the 150 nm thick gold film. We noticed small gold particles around the aperture edge. Nanoscale particles and fibers were also found at the border of the gold cap. Right: SEM image of a single 230 nm aperture within a 6×6 array. This aperture was exempt of nearby gold particles.
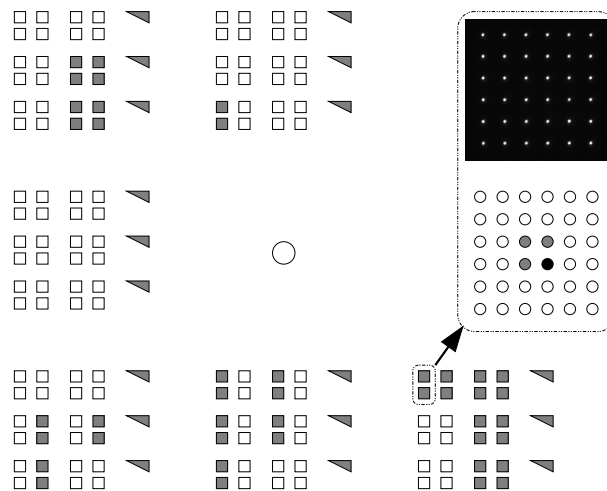


Fig. 2. Mask layout with orientation triangles and aperture arrays. Every square represents an array with 6×6 apertures of identical diameter. In each array, the apertures are located on a square grid with 5 $\mu$m period. We selected 21 array pairs in order to cover aperture diameters between 115 nm and 520 nm. Inset: Trans-illumination image and scheme of an array pair with 2×6×6 apertures of 300 nm diameter in the 150 nm gold film. The central apertures in the selected arrays were measured with FCS.

## 2.2. Experimental setup and measurements

Figure 3 outlines our confocal trans-illumination setup with a piezo *xyz*-translation stage (New-port ULTRAlign 561D with $\mu$Drive Controller ESA-C) for the sample positioning. A 12 mW HeNe gas laser (Laser 2000 LHRP-1201, linearly polarized) and a laser-line clean-up filter (Chroma Z633/10x) provided a spectrally pure 633 nm excitation. The beam was expanded to fill the aperture of a Carl Zeiss 40x0.90 NA water immersion objective. The beam waist in the focus was 350 nm. Neutral density filters (Thorlabs NDK01) were used to adjust the power in the excitation volume. The fluorescent light was collected with a 40x1.20 NA water immersion objective (Carl Zeiss) and filtered by a dichroic mirror (Chroma Q660LP), a band-pass filter (Chroma HQ710/100m) and a pinhole (Thorlabs ASFxx/125Y step-index fibers: 37.5 $\mu$m, 50 $\mu$m or 100 $\mu$m core diameter). The pinhole provided a spatial filtering, hence contributing to the background rejection as well as to the limitation of the detection volume. A single photon counting module (PerkinElmer SPCM-AQR-14-FC) detected the fluorescence photons. The signal (number of photons over time) was correlated with a USB hardware correlator (Correlator.com Flex99OEM-12C) attached to a standard PC. The liquid sample, sandwiched between the aperture mask and a microscope slide, was positioned with the mask in the focal plane.
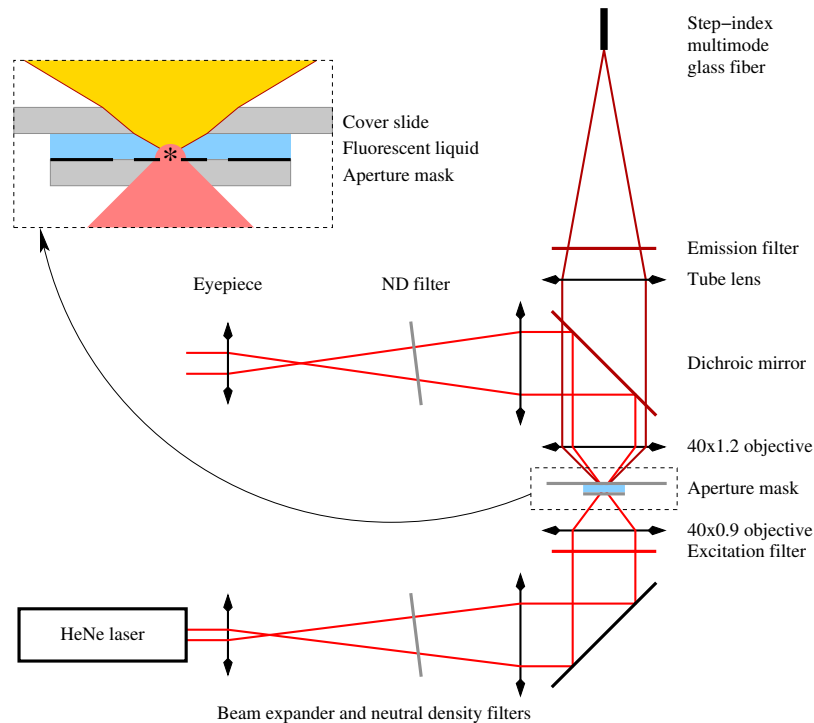


Fig. 3. Confocal trans-illumination setup. The 40x0.9 objective and the multimode fiber were mounted on *xyz*-translation stages. The aperture mask was aligned with a piezo *xyz*-translation stage.

## 3. Theory

The FCS and FFS theory was recently reviewed by Krichevsky et al. [19]. Following the general ideas, the fluorescence intensity $I_{(t)}$ is correlated during a time interval $T$. The symmetrically

normalized auto-correlation function is defined as

$$G_{(\tau)} = \frac{\langle I_{(t)} I_{(t+\tau)}\rangle}{\langle I_{(t)}\rangle\langle I_{(t+\tau)}\rangle} = (T - \tau)\frac{\int\limits_0^{T-\tau} I_{(t)} I_{(t+\tau)}\, \mathrm{d}t}{\int\limits_0^{T-\tau} I_{(t)}\, \mathrm{d}t \int\limits_\tau^T I_{(t)}\, \mathrm{d}t} \tag{1}$$

The auto-correlation $G_{(\tau)}$ allows to extract essential single molecule parameters from the fluctuating fluorescence intensity. Typical fluctuation sources are diffusion (Brownian motion) of fluorescent particles through the detection volume; emission characteristics like triplet state occupation; or changes of the molecular conformation influencing the emission characteristics. The correlation amplitude is inversely proportional to the number of fluctuation sources (particles) in the detection volume. The shape of the correlation curve encodes all these processes, whereas the time dependencies modify the corresponding time windows.

### 3.1. Excitation field

Figure 4 shows the excited fields for three different aperture diameters calculated with the Green's tensor technique [14]. We simulated the transmission of a Gaussian beam through the apertures in the gold film. The Gaussian beam had a wavelength of 633 nm and was linearly polarized along the $x$-axis corresponding to the HeNe laser. In the glass substrate with a refractive index of 1.52, it was focused and centered on the bottom of the aperture. The transmission for an incident beam waist $w_0 = 350$ nm was simulated. In the aperture and on top of the gold film, we set the refractive index to 1.33 for water. The relative dielectric constant of the gold film was $-11.6 + 1.26i$.
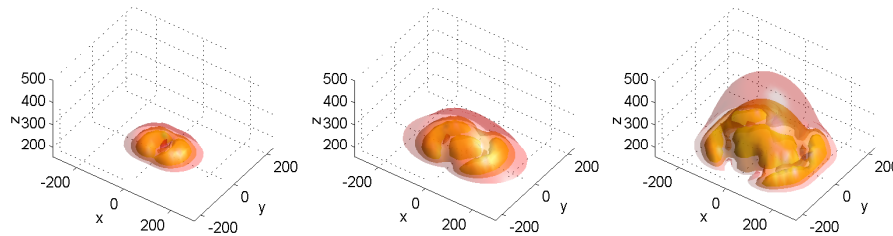


Fig. 4. Simulated excitation fields for aperture diameters of 150 nm (left), 250 nm (center) and 400 nm (right) in a gold film of thickness $h = 150$ nm. All dimensions are given in nanometers. The coordinate origins are located in the center at the bottom of each aperture. A Gaussian beam with 633 nm wavelength was focused with an opening angle equivalent to a numerical aperture of 0.6 on the apertures. The graphs show three surfaces of equal intensity at $e^{-1}I_{max}$ (inner surfaces), $e^{-1.5}I_{max}$ (middle surfaces) and $e^{-2}I_{max}$ (outer surfaces). $I_{max}$ is the maximal excitation intensity at $z = h$. On top of the apertures, the average intensity was reduced to 22%, 73% respectively 87% of the incident intensity at the bottom.

For the 400 nm aperture, the excitation field is similar to the focus of the Gaussian beam. The aperture mainly truncates the tails of the Gaussian beam and diffraction shrinks the vertical extension to 330 nm after the hole. In the close vicinity of the aperture, the excitation field shows a fine structure reflecting the $x$-polarization of the incident beam and the wave modes in the aperture. With the 250 nm aperture, the $y$-extension of the excitation volume is slightly smaller, whereas the $z$-dimension is reduced significantly. This effect is even more important for the 150 nm aperture, where the excitation field extends only 80 nm into the liquid. Table 1 compares the extensions of the ellipsoid-like excitation fields and the estimated volumes. We

estimated the excitation volume $V_{ex}$ with $W_1$ [22] and the effective sampling volume $V_{eff}$ for FCS with $W_1^2/W_2$, where

$$W_n = I_{max}^{-n} \iiint I_{(\vec{r})}^n \, \mathrm{d}\vec{r} \tag{2}$$

Here, we approximated the product of the excitation intensity and the detection efficiency by the excitation intensity alone. This is valid because the excitation intensity drops much faster than the detection efficiency, if $\vec{r} \to \infty$. In both cases, we added the aperture volume $V_{ap} = \pi h d^2/4$, where $h = 150$ nm is the aperture depth and $d$ the diameter.

Table 1. Calculated extensions of the excitation fields along the $x$, $y$ and $z$ axes, respectively excitation volumes $V_{ex} = W_1 + V_{ap}$ and effective sampling volumes $V_{eff} = W_1^2/W_2 + V_{ap}$ for different aperture diameters $d$. The extensions are understood as $e^{-2}$ "half-axes" for comparison with the $e^{-2}$ $xy$-waist $w_0 = 350$ nm of the incident beam.

| $d$ | 150 nm | 250 nm | 400 nm | $\infty$ * | $\infty$ ◇ | $\infty$ ° |
|---|---|---|---|---|---|---|
| $w_x$ | 140 nm | 240 nm | 230 nm | 350 nm | 250 nm | 180 nm |
| $w_y$ | 100 nm | 140 nm | 200 nm | 350 nm | 250 nm | 180 nm |
| $w_z$ | 80 nm | 160 nm | 330 nm | 2.0 $\mu$m | 1.0 $\mu$m | 700 nm |
| $V_{ex}$ | 6.7 al | 17 al | 38 al | 130 al | 130 al | 55 al |
| $V_{eff}$ | 27 al | 64 al | 130 al | 480 al | 590 al | 250 al |

\* At the glass surface without aperture. In free liquid, $V_{ex} = 260$ al and $V_{eff} = 960$ al.
◇ State-of-the-art in free liquid for 633 nm wavelength [20].
° State-of-the-art in free liquid for 488 nm wavelength [20].

We would like to emphasize that diffraction and interference generate these highly confined excitation fields. In $\vec{k}$-space, diffraction creates a transverse component $k_{xy}$ parallel to the $xy$-plane. Because the length of the wave vector $\vec{k}$ is constant, $k_z$ has to adopt according to

$$k_z^2 = k^2 - k_{xy}^2 \tag{3}$$

Sub-wavelength sized apertures enforce $k_{xy} > k$ resulting in an imaginary $k_z$. This gives the transmitted field a dominant evanescent field character along the $z$-axis. The vertical extension $w_z$ decreases with the aperture diameter. Moreover, the lateral extensions decrease due to destructive interference of many surface waves with different $k$. A simulation at identical conditions but at a wavelength of 488 nm showed that the excitation field *grows* along the $z$-axis. Using sub-wavelength sized apertures, we took advantage of diffraction to obtain highly confined excitation fields below the far-field diffraction limit.

### 3.2. Auto-correlation model equation

As an approximation, we used the standard model equation for free diffusion of a single fluorescent species through a sampling volume with a 3D Gaussian shape [21, 22]. We modeled the normalized auto-correlation $G_{(\tau)}$ by

$$G_{(\tau)} = G_\infty + \left(1 - \frac{I_B}{\langle I \rangle}\right)^2 \frac{\gamma}{N} \left\{ \left(1 + \frac{\tau}{\tau_d}\right)^{-1} \left(1 + \frac{\tau}{K^2 \tau_d}\right)^{-1/2} + \frac{P_t}{1 - P_t} \exp\left(-\frac{\tau}{\tau_t}\right) \right\} \tag{4}$$

$G_\infty \approx 1$ is the correlation amplitude in the long lag time limit $\tau \to \infty$, $N$ is the average number of molecules in the sampling volume, $\tau_d$ is the lateral diffusion time, $K$ is the ratio of axial over

lateral extension of the sampling volume, $P_t$ is the probability of molecules in the triplet state and $\tau_t$ is the correlation time of this triplet state population. $I_B$ is the background count rate and $\langle I \rangle$ is the mean count rate (fluorescence intensity and background). In our case, we assumed $\gamma$ to be 1/2 because the mask cuts half of the sampling volume [12]. Figure 5 shows typical correlation amplitudes for different aperture diameters. For apertures larger than 250 nm, Eq. (4) yielded good results. For smaller apertures, the auto-correlations had a significant tail for lag times $\tau$ between 0.1 ms and 1 ms. We attribute the tail to constrained diffusion in the aperture,
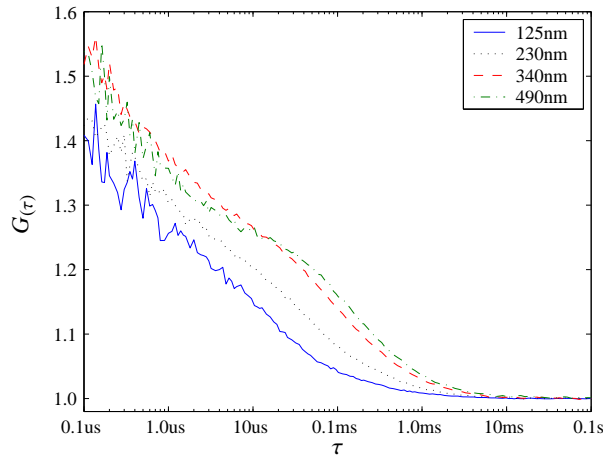


Fig. 5. Afterpulsing corrected auto-correlations $G_{(\tau)}$ versus lag time $\tau$ for aperture diameters of 125 nm, 230 nm, 340 nm and 490 nm at a Cy5 concentration of 12 nM. The correlation amplitude for the 490 nm aperture was multiplied by 3. For the 125 nm and the 230 nm aperture, the correlation amplitudes show a different slope for delays between 0.1 ms and 1 ms. We interpret this as constrained diffusion of molecules entering into the 150 nm deep aperture.

i.e. molecules entering into the 150 nm deep aperture were laterally captured for some time interval. Therefore, they needed more time to diffuse out of the sampling volume. The boundary conditions for Eq. (4) are not taking into account this trapping inside the aperture. This leads to a mismatch if the fit is based on Eq. (4). Figure 6 shows fits and residuals for measurements at a Cy5 concentration of 30 nM. In free liquid and for the 490 nm aperture, Eq. (4) fits well with low residuals. For the 125 nm aperture, Eq. (4) leads to significant residuals and even a bias at large lag times. Nevertheless, the extracted diffusion time $\tau_d$ is a good approximation because it accounts only for the diffusion in the $xy$-plane. Also, the number of molecules $N$ depends mainly on the correlation amplitude $G_{(0)}$ and the triplet probability. Therefore, it does not change significantly for different diffusion models.

### 3.3. Evaluation of the auto-correlation

For analyzing the experimental auto-correlation curves, we corrected the correlation amplitude for afterpulsing to avoid a systematic bias on short diffusion times. Figure 7 shows how afterpulsing affected the auto-correlation amplitude up to a lag time $\tau \approx 10$ $\mu$s. According to Bismuto et al. [23], we estimated the afterpulsing contribution by averaging auto-correlations $G_{uc}$ for an uncorrelated source (daylight). For minimizing the discrepancies between the curves, we introduced an exponent for the mean count rate $\langle I_{uc} \rangle$.

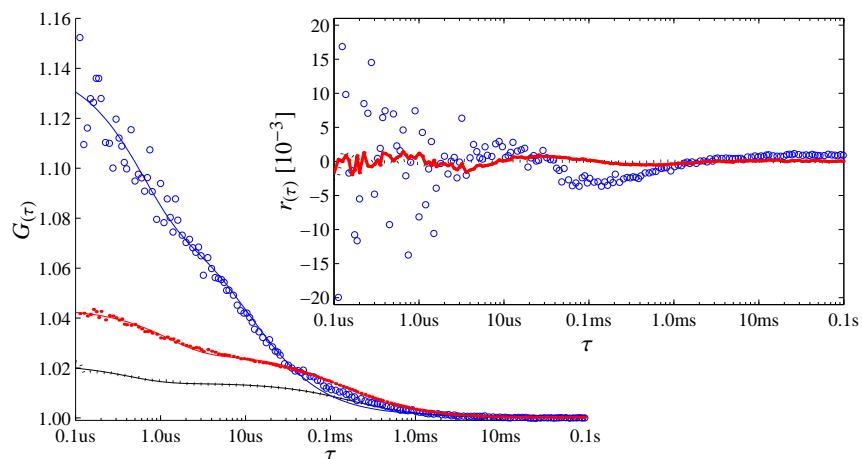$$G_{ap(\tau)} = \left\langle (G_{uc(\tau)} - 1) \langle I_{uc(t)} \rangle^{1.02} \right\rangle \tag{5}$$

Fig. 6. Auto-correlations and fits $G_{(\tau)}$ versus lag time $\tau$ for aperture diameters of 125 nm (blue circles), 490 nm (red points) and for free liquid (black dotted) at a Cy5 concentration of 30 nM. Inset: Fit residuals $r_{(\tau)} = G_{fit}/G_{(\tau)} - 1$.

Subtracting the estimated afterpulsing contribution $G_{ap}/\langle I \rangle^{1.02}$ prior to parameter extraction allowed to analyze diffusion times shorter than 20 $\mu$s accurately. The model parameters were extracted by fitting the curves with Eq. (4) on the measured auto-correlations. For fitting, we used a non-linear least-squares algorithm (multidimensional Gauss-Newton algorithm). The background count rate $I_B$ and the mean count rate $\langle I \rangle$ were measured directly.
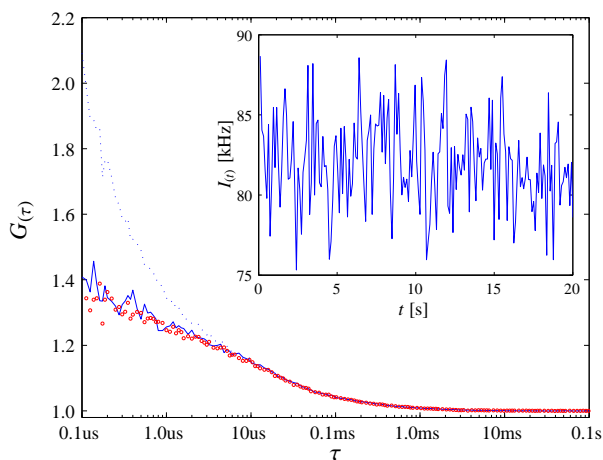


Fig. 7. Auto-correlations $G_{(\tau)}$ versus lag time $\tau$ measured on a 125 nm aperture at a Cy5 concentration of 12 nM. The blue dotted line is the measured auto-correlation. The solid line shows the afterpulsing corrected amplitude. The circles trace a second measurement on the same aperture. Inset: intensity trace.

## 3.4. Prediction of FCS results

In case of free diffusion, the diffusion time $\tau_d$ is given by $w_0^2/4D$ where $w_0$ is the lateral beam waist and $D$ the diffusion constant [22]. In our case, the extension of the sampling volume is

limited by the excitation field, which in turn is restricted by the diameter $d$ of the aperture. Figure 5 suggests proportionality of the diffusion time and the aperture diameter. Based on our calculations, we expect to find $\tau_d \propto d^2$ for small apertures. For large apertures, the sampling volume is given by the beam waist $w_0$ and the diffusion time levels off to some value $\tau_\infty$, which might be different from $\tau_d$ due to surface effects. Overall, we assume to get a behavior as

$$\tau_d \approx \tau_\infty \frac{d^2}{d_\tau^2 + d^2} \tag{6}$$

where $d_\tau$ marks the transition between the small and the large aperture regime. Equation (6) is understood as a first approximation of the effective relationship between $\tau_d$ and $d$.

The number of molecules $N$ is determined by the effective sampling volume $V_{eff}$ and the fluorophore concentration $C$.

$$N = CN_A V_{eff} \tag{7}$$

Here, $N_A = 6.022 \times 10^{23}$ mol$^{-1}$ is the Avogadro number. For small apertures, the sampling volume increases with the aperture diameter as shown in table 1. For large apertures, the sampling volume gets constant because the excitation field is no longer constrained by the aperture. Therefore, we expect a relationship similar to Eq. (6) between $N$ and $d$.

## 4. Results and discussion

For the mask layout shown in Fig. 2, we selected 21 array pairs to cover 21 aperture diameters from 115 nm to 520 nm. Figures 8–11 summarize the results for a 150 nm gold mask on a 150 $\mu$m glass substrate. A 12 nM respectively 30 nM solution of Cy5 (Molecular Probes) was excited at 633 nm. We kept the laser power constant at 0.3 mW incident onto the apertures.

### 4.1. Diffusion time

For a concentration of 12 nM, we measured with a 38 $\mu$m, a 50 $\mu$m and a 100 $\mu$m pinhole diameter. Figure 8 shows the diffusion time versus the aperture diameter. For the 115 nm apertures, the diffusion time was around 15 $\mu$s. It increased with the aperture diameter and reached 140 $\mu$s for the 500 nm apertures. On the 400 nm apertures, we measured $\tau_d \approx 100$ $\mu$s against 20 $\mu$s on the 150 nm apertures. This ratio of 1/5 is in good agreement with the calculated ratio of 1/4 for these aperture diameters.

The pinhole diameter had no significant influence on the measured diffusion time. With the 40× objective and the 38 $\mu$m pinhole, we got a projected pinhole diameter of roughly 1 $\mu$m in the mask plane, which was still much larger than the largest aperture. Our measurements show that the excitation volume was effectively smaller than the detection volume, which underlines the insensitivity to pinhole diameter variations. Also, we see that an increase of the fluorophore concentration to 30 nM did not significantly change the measured diffusion time. Only for aperture diameters above 300 nm, a slight increase was measured. We attribute this to detector saturation leading to a virtually increased sampling volume. Figure 10 shows that the detector was driven at more than 1.0 MHz for apertures larger than 300 nm. At these count rates, the detector death time of 50 ns started to become significant – particularly during photon bursts – and biased the FCS results [24].

Overall, Eq. (6) is well reproduced with a transition diameter $d_\tau$ of 450 nm and a diffusion time limit $\tau_\infty$ of 240 $\mu$s. Including the lateral penetration of the excitation light into the aperture walls, the excitation field had a diameter of about 500 nm at $d_\tau$. In agreement with Eq. (6), $d_\tau$ marked the aperture diameter yielding 1/2 of the beam cross-section $\pi w_0^2$. In free liquid, we measured a diffusion time $\tau_d \approx 160$ $\mu$s. When the confocal volume was placed at the cover slide
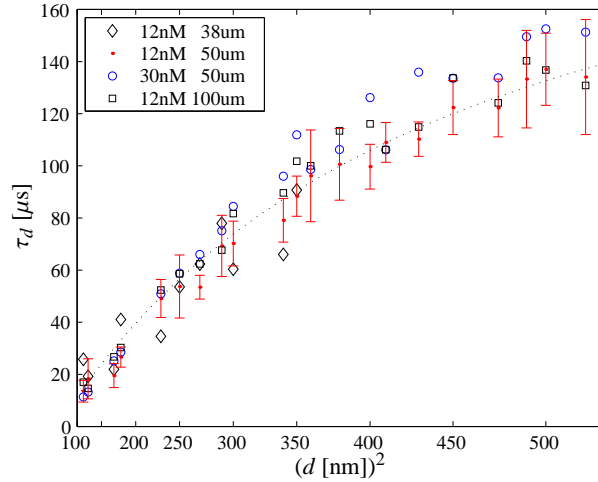
Fig. 8. Diffusion time $\tau_d$ versus aperture diameter $d$. The data points show the average and the error bars the standard deviation of 10 measurements per aperture diameter. For clarity, the standard deviation is shown for one case only (12 nM Cy5, 50 $\mu$m pinhole). The black dotted line was calculated with Eq. (6) for $\tau_\infty = 240\ \mu$s and $d_\tau = 450$ nm. In free liquid, the diffusion time was 160 $\mu$s to 170 $\mu$s. Inset: concentration of Cy5 and pinhole diameter of all cases.

surface, $\tau_d$ reached 250 $\mu$s to 300 $\mu$s, which is consistent with $\tau_\infty$. For the smallest apertures, $\tau_d$ was less than 1/10 of the value measured in free liquid. We conclude that the introduction of the 115 nm apertures reduced the lateral extension of the excitation volume to less than 1/3. Hence, the measured diffusion times indicate a reduction of the sampling volume to less than 1/10 of the conventional confocal volume.

### 4.2. Number of molecules

For a Cy5 concentration of 30 nM, we show the number of molecules obtained by fitting the afterpulsing corrected auto-correlations in Fig. 9. For an aperture diameter of 115 nm, we measured about 3 molecules in average in the sampling volume. Increasing the aperture diameter to 350 nm increased the number of molecules to about 12. Then, the number of molecules leveled off between 14 and 18 for larger apertures, which was roughly 1/4 the value in free liquid. The measured ratios of the number of molecules for the 150 nm, 250 nm and 400 nm apertures are close to the calculated ratios of the sampling volumes $V_{eff}$ in table 1.

In contrast to the diffusion time, the number of molecules is affected by the background contribution of each individual aperture. Therefore, we measured first the background on each aperture with pure water. With the Cy5 solution, we measured these apertures again. However, it was virtually impossible to mutually realign the confocal volume and the apertures identically. Therefore, the excitation intensities differed by as much as 20% resulting in a 40% variance in the background corrected number of molecules. This made it difficult to measure the sampling volume for an individual aperture.

### 4.3. Signal to noise ratio

Figure 10 shows the background, the mean intensity and the SNR measured during the experiment described in subsection 4.2. The mean intensity increased with $d^2$ from about 90 kHz on the 115 nm apertures to 1.8 MHz on the largest apertures. On the other hand, the background
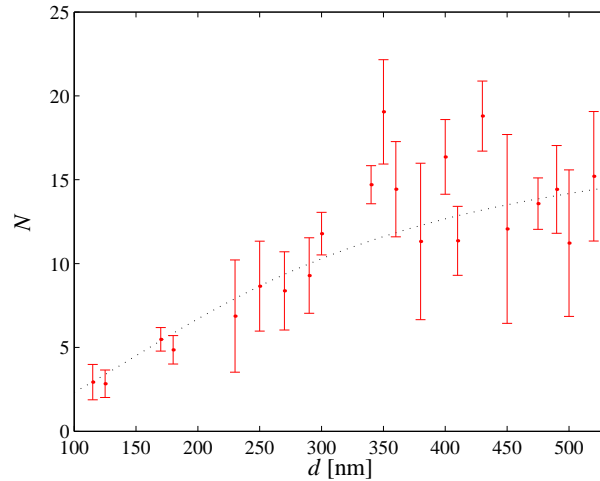
Fig. 9. Number of molecules $N$ versus aperture diameter $d$ for a Cy5 concentration of 30 nM and a 50 $\mu$m pinhole. The data points show the average and the error bars the standard deviation of 10 measurements per aperture diameter. The dotted line is for guiding the eyes. In free liquid, we measured about 72 molecules in the confocal volume.

depended very much upon the state of individual apertures. Its standard deviation was particularly low for apertures smaller than 200 nm. Thereby, despite the small signal, we were able to predict and correct background accurately for these apertures.
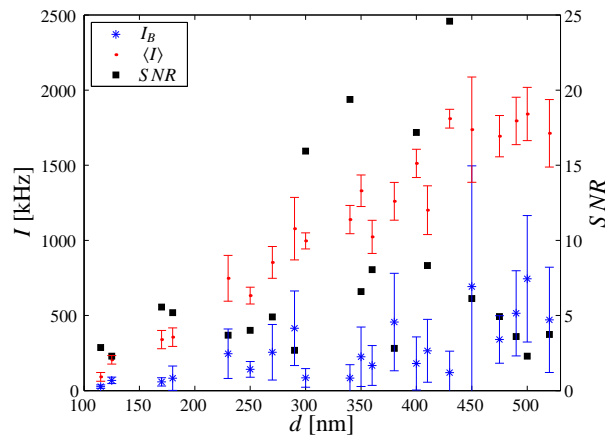


Fig. 10. Background count rates $I_B$, mean intensity $\langle I \rangle$ and $SNR = \langle I \rangle / I_B - 1$ versus aperture diameter $d$ for a Cy5 concentration of 30 nM and a 50 $\mu$m pinhole. The data points show the average and the error bars the standard deviation of 10 measurements per aperture diameter. In free liquid, we measured an intensity of 4.7 MHz and a background of 6 kHz.

For aperture diameters up to 200 nm, we measured SNRs between 2.5 and 6. The best results were obtained with aperture diameters of 300 nm, 340 nm and 430 nm with corresponding SNRs of 16, 19, respectively 25. Typically, conventional instruments provide a SNR > 50 (2 kHz background, 100 kHz to 500 kHz mean intensity). By increasing the Cy5 concentration, we could reach a SNR > 10 for aperture diameters up to 200 nm. In our experiment, the SNR

was limited by the large background, which was mainly due to photo-luminescence of the gold [25] and the glass slide; surface enhanced Raman scattering [26] of water molecules, particularly at the aperture edge; and fluorescence of photo-resist residues if any. By mastering the lithography process, we could remove any photo-resist residue. For reducing the background further, we compared the photo-luminescence of different materials. For instance, we measured the photo-luminescence of silver and found it an order of magnitude lower than for gold. Nevertheless, we kept using gold for greater compatibility with biological applications (surface chemistry).

### 4.4. Count rate per molecule

Figure 11 shows the CPM obtained from the experiment described in subsection 4.2. Starting at about 23 kHz for the 115 nm apertures, the CPM increased quickly to about 61 kHz for the 250 nm apertures. Then, there was only a slight increase to about 82 kHz for the 400 nm apertures. This behavior qualitatively follows the calculated excitation intensities. The intensity on top of the 250 nm aperture is about 3.3 times the intensity of the 150 nm aperture, but only about 12% lower than for the 400 nm aperture.
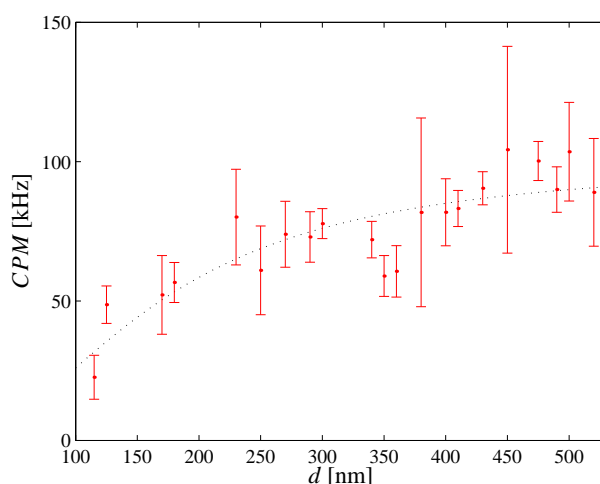


Fig. 11. Background corrected count rate per molecule *CPM* versus aperture diameter *d* for a Cy5 concentration of 30 nM and a 50 $\mu$m pinhole. The data points show the average and the error bars the standard deviation of 10 measurements per aperture diameter. The dotted line is for guiding the eyes. In free liquid, we obtained a *CPM* $\approx$ 65 kHz for this experiment.

If we compare the values for the large apertures, we notice that the count rates per molecule exceed the values measured in free liquid. We interpret this by the mirror effect of the gold film, which reflects a significant part of the fluorescent light emitted towards the aperture and the gold film. In particular, the emission under high incidence angles falls onto the gold film surrounding the aperture and is efficiently reflected back into the objective. For instance, we measured a CPM of 103 kHz in case of the 500 nm apertures exceeding the CPM in free liquid by 60%.

## 5. Conclusions

We demonstrated that FCS on single apertures is an interesting approach for molecular investigations at 10 nM to 100 nM concentration. Using apertures of various sizes, we calculated

and engineered the excitation field. For small apertures, we verified that the diffusion time and the number of molecules are proportional to the aperture diameter. We measured a reduction of the effective sampling volume by an order of magnitude compared to the typical volume in confocal FCS.

The background on individual apertures was hard to predict, particularly for the large apertures. Therefore, we encountered some difficulties measuring the number of molecules and the count rate per molecule accurately. Nevertheless, the average values confirmed our calculations. In particular, we could report comparable or even higher count rates per molecule than in confocal FCS. Using homogeneous aperture arrays and an optimal combination of materials, excitation wavelength and power, we expect to measure all FCS parameters accurately.

We would like to point out that confocal trans-illumination FCS performs nearly as well as confocal epi-illumination FCS. With trans-illumination, the excitation light falls directly onto the detection pinhole. Therefore, the emission filter has to block the full excitation power instead of the small fraction of backscattered light. This results in a somewhat higher background but can be compensated by using two microscope objectives on either side of the sample, therewith doubling the detection efficiency. Finally, the alignment of the excitation and detection volumes is more precise since the small aperture serves as a common pinhole.

**Acknowledgements**